ACS Photonics

Article

pubs.acs.org/journal/apchd5

Magnetoplasmonic Faraday Rotators: Enabling Gigahertz Active Polarization Control for Integrated Plasmonics

Curtis J. Firby,*[,†] PoHan Chang,[‡] Amr S. Helmy,[‡] and Abdulhakem Y. Elezzabi[†]

[†]Ultrafast Optics and Nanophotonics Laboratory, Department of Electrical and Computer Engineering, University of Alberta, Edmonton, Alberta T6G 1H9, Canada

[‡]The Edward S. Rogers Sr. Department of Electrical and Computer Engineering, University of Toronto, Toronto, Ontario M5S 3G4, Canada

ABSTRACT: We present the design and theoretical characterization of a magnetoplasmonic Faraday rotator for active polarization control in integrated plasmonics. By incorporating bismuth-substituted yttrium iron garnet (Bi:YIG) into a unique hybrid ridge−plasmonic waveguide structure, we effectively overcome the phase-matching limitations between photonic TE and plasmonic TM modes, and hence attain efficient Faraday rotation within a plasmonic device. The device provides 99.4% polarization conversion within a length of 830 μm, while the two modes exhibit propagation lengths in excess of 1 mm. This versatile optical building block can be operated with either a TE or TM input, making it ideal for polarization switching and polarization division multiplexing. Additionally, a buried Ag transmission line under the waveguide facilitates high-speed active polarization modulation by generating transient magnetic fields and modulating the Bi:YIG magnetization. We show that with these transient fields and an external static biasing field one can operate the device in either a pulsed-input pulsed-output mode, to produce a polarization switch, or a pulsed-input continuous-output mode, to produce a polarization oscillator. Such a device is shown to be capable of polarization modulation of 10 GHz and will be vital in realizing plasmonic circuits employing polarization diversity.

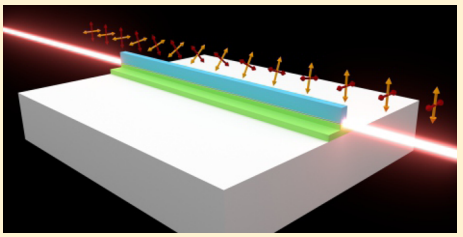

KEYWORDS: *magnetoplasmonics, Faraday effect, polarization rotation, integrated optics, magnetization dynamics, Bi:YIG*

Polarization control is fundamental to optical signal processing and integrated optical networks. Specifically, polarization division multiplexing, whereby optical signals of orthogonal polarization states are passed through a waveguide or fiber simultaneously, doubles the transmission bandwidth of a communications network.[1] In combination with an external polarizer, altering the polarization state is an effective means of modulating the intensity of an optical signal as well.[2,3] Accordingly, polarization-controlling and -manipulating devices have been a subject of great interest.[4,5] As integrated optical technology progresses toward the plasmonic regime, polarization state management is increasingly critical, due to the extreme sensitivity of nanoplasmonic devices to an incident lightwave's polarization.

Current polarization manipulating devices utilizing plasmonics can typically be classified into two categories: planar metasurface structures and waveguide-based devices. The metasurface approach involves the precise design of plasmonic nanoantenna arrays or arrays of subwavelength apertures in a metallic film to control the amplitude and phase of the reflected or transmitted electric fields.[6−9] However, these designs are intended as free space components, and thus are not suited for integrated photonics applications.

Alternatively, waveguide-based designs are much more amenable for integrated operation and have been extensively examined for silicon photonics.[10,11] There have been several approaches to this class of plasmonic mode converting device, involving either mode evolution or mode interference. In a plasmonic mode evolution device, the structure is designed to have a gradually changing metal feature, such that the input mode couples to a plasmon on the metal and adiabatically evolves into the desired output polarization state. This includes metal tapers,[12,13] shifted metal caps,[14] or metallic claddings that wrap around the edge of the waveguide,[15,16] often employed in conjunction with tapered dielectric cores. Plasmonic devices of this type have been used to convert between orthogonal photonic mode polarizations[12,15,16] or to convert between a TE photonic mode and a TM plasmonic mode.[13,14] On the other hand, mode interference-based devices are composed of an asymmetric structure that rotates the symmetry axis of the waveguide. As such, a pure TE or TM input mode decomposes into two hybrid modes, which interfere along the length of the device. Examples of this type of device include dielectric cores covered by a metallic film on two adjacent sides[17,18] or a thin metallic strip covering a fraction of the top of the guide.[19,20] While both these classes of plasmonic devices can be very short (i.e., <10 μm), both approaches are inherently passive in nature, as the mode conversion is fixed for a particular device length. More importantly, even though the aforementioned devices can be designed for passive polarization manipulation, the lack of time reversal symmetry breaking makes them unable to achieve

Received: July 22, 2016
Published: November 15, 2016

DOI: 10.1021/acsphotonics.6b00523
ACS Photonics 2016, 3, 2344−2352

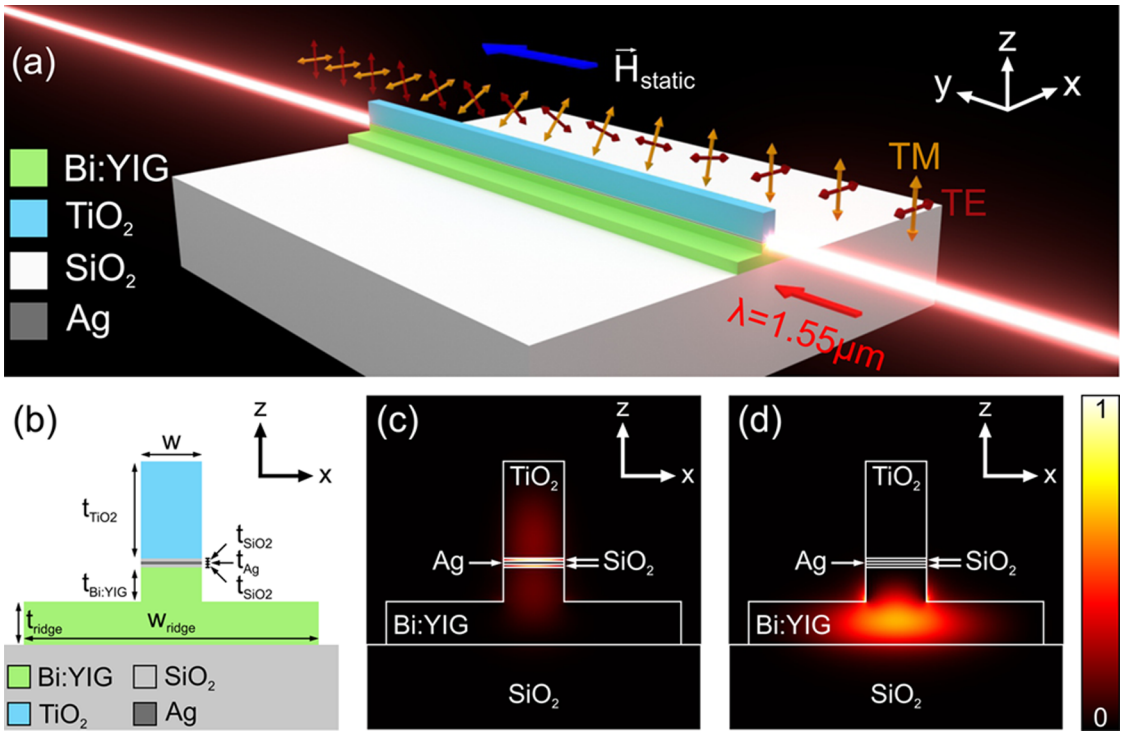

Figure 1. (a) Illustration of the magnetoplasmonic Faraday rotator under consideration. The device is capable of rotating the polarization of either a TE or TM input mode. (b) Schematic diagram of the hybrid ridge−plasmonic waveguide structure. (c) $|E_z|^2$ profile for the TM plasmonic mode supported by the structure. (d) $|E_x|^2$ profile for the TE photonic mode supported by the structure.

nonreciprocal operation such as optical isolation, circulation, or one-way transmission. For chip-scale integrated plasmonics, a versatile polarization manipulation platform that can be configured dynamically for the desired applications and exhibits nonreciprocal propagation behavior is of great necessity. Such a platform must facilitate an active and tunable mechanism of polarization/mode conversion for encoding signals and switching polarization states within an optical network.

To meet these demanding performance requirements, the aforementioned structural rotation configurations cannot be utilized, and material-based mechanisms must be considered. A method of achieving this tunable and active functionality can be realized by invoking the properties of magneto-optic (MO) materials. Notably, light propagating through a MO medium magnetized along the direction of propagation will be subject to the Faraday effect, whereby the polarization is rotated as the lightwave passes through the material. Inducing such gyrotropy within an integrated waveguide converts a TE mode to TM, or vice versa, as has been demonstrated within rib waveguides for large-scale photonics.[21] This phenomenon is capable of providing high-speed active control, as the Faraday effect is induced by the material's magnetization, which can be altered through the application of external magnetic fields. Incorporating this effect into plasmonic structures is of paramount interest, as this would provide a crucial mechanism of controlling polarization at the nanoscale. Additionally, the MO-based Faraday rotator can then be cascaded between a series of polarizers to achieve large discrimination of propagation loss between forward and backward incidence, which serves as the most fundamental component for an integrated Faraday isolator.

Within the field of magnetoplasmonics,[22,23] demonstrations of the Faraday effect have been limited. Specifically, the few presentations involve the enhancement of polarization rotation for light transmitted through Au nanowire gratings on a magnetic substrate,[24,25] Au nanoparticles embedded in a magnetic garnet matrix,[26] or a perforated metallic film incorporating magnetic materials within either the subwavelength apertures[27] or the perforated film itself.[28] However, to date there has been no presentation of a waveguide-based plasmonic Faraday rotator. This is due to the fact that the mode conversion efficiency is strongly dependent upon matching the phase velocities of the photonic TE and plasmonic TM modes of the structure. In typical plasmonic waveguides, the effective index difference between the TE and TM modes is considerable, and thus, conversion efficiencies are limited. Additionally, optical modes in close proximity to metallic features are limited by their finite propagation length, while mode conversion due to the Faraday effect typically occurs on a length scale of several hundred micrometers to millimeters. Thus, one requires a structure capable of supporting low-loss, long-range, phase-matched TE and TM modes. These stringent constraints have proven to be formidable to simultaneously overcome, and thus far no progress has been made in this area.

Here, we present a solution to this dilemma, utilizing a Faraday rotator configuration for active polarization control in integrated plasmonics. Through the implementation of a unique hybrid ridge−plasmonic waveguide structure composed of bismuth-substituted yttrium iron garnet (Bi:YIG), the TE and TM modes within the structure are effectively phase matched, while maintaining millimeter-scale propagation lengths. Magnetizing this device provides 99.4% mode conversion within a length of 830 μm via the Faraday effect. To achieve high-speed dynamic polarization control, the inclusion of a nearby transmission line allows magnetic field transients to manipulate the magnetization of the Bi:YIG and

DOI: 10.1021/acsphotonics.6b00523
ACS Photonics 2016, 3, 2344−2352

thus the output polarization state. We show this active device to be operable in two dynamic modes, producing modulated output up to 10 GHz. The underlying hybrid ridge−plasmonic architecture can represent a new avenue toward modal phase-matching engineering for plasmonic integrated circuits.

MO WAVEGUIDE DESIGN AND PASSIVE OPERATION

The waveguide structure for a magnetoplasmonic Faraday rotator must simultaneously facilitate long-range plasmonic and photonic modes, as well as a mechanism of achieving phase matching between them. To attain this, we conceived a unique hybrid ridge−plasmonic waveguide design, schematically depicted in Figure 1a,b, which combines functionalities of both five-layer hybrid plasmonic structures and standard ridge waveguides. Through judicial engineering of the hybrid plasmonic waveguide dimensions, one can generate a nearly symmetric transverse field component (E_z in this geometry) on either side of the metallic film, effectively minimizing the modal overlap with the metal and therefore reducing the losses for the TM plasmonic mode.[29] Notably, this design does not demand a vertically symmetric geometry or material profile, as the layer thicknesses can be tailored for field symmetry, and hence minimum losses.[29] Thus, such a design allows for the customization of a long-range TM plasmonic mode, as depicted in Figure 1c.

To form this mode within the present structure, the multilayer stack is chosen to be w = 450 nm wide, the metal is chosen to be a t_{Ag} = 25 nm thick film of Ag, and the two low-index layers consist of t_{SiO_2} = 20 nm thick films of SiO_2. The refractive indices (at λ = 1.55 μm) of these layers are taken to be $n_{Ag} = 0.145 + 11.438i$[30] and $n_{SiO_2} = 1.444$,[31] respectively. The top high-index layer of the structure is chosen to be a t_{TiO_2} = 725 nm thick layer of amorphous TiO_2, as TiO_2 has a refractive index of $n_{TiO_2} = 2.3 + 1.1 \times 10^{-6}i$ at λ = 1.55 μm.[32] The high-index bottom film and the ridge sit atop SiO_2 and are constructed from Bi:YIG, where t_{ridge} = 320 nm and $t_{Bi:YIG}$ = 260 nm. It is within this MO region that the TE and TM modes must exhibit overlap for the Faraday rotation to occur.

Notably, the ferrimagnetic garnet, Bi:YIG, is ideal for implementation into this hybrid ridge−plasmonic structure, due to its high refractive index of $n_{Bi:YIG}$ = 2.3 at λ = 1.55 μm.[33] Such a material can be modeled as lossless due to its transparency window in the infrared telecom band. Ferrimagnetic garnets have recently found widespread use in magneto-plasmonic waveguide devices, as their magnetization can be saturated with low magnetic fields (i.e., a saturation magnetization of $\mu_0 M_S$ = 9 mT),[33] and they exhibit low Gilbert damping parameters (i.e., $\alpha = 10^{-4}$).[34] Additionally, they display sizable MO effects with a large specific Faraday rotation of $\theta_F = 0.25°/\mu m$ at λ = 1.55 μm,[33] and their magnetization can respond to ultrafast magnetic field transients.[35]

The operation of this device requires a delicate balance between the modal losses and the modal overlap required for efficient Faraday rotation. To achieve long-range propagation from a TE mode in a structure with a lossy metal film, the overlap of the TE mode with the metal must be reduced while maintaining overlap with the TM mode fields inside the MO material required for mode conversion. This is possible with the inclusion of the Bi:YIG ridge at the base of the hybrid plasmonic guide, which shifts the TE mode away from the metal, as shown in Figure 1d. Increasing the width of the ridge effectively reduces the loss of the TE mode, as illustrated in Figure 2a. Furthermore, this ridge structure provides a means of

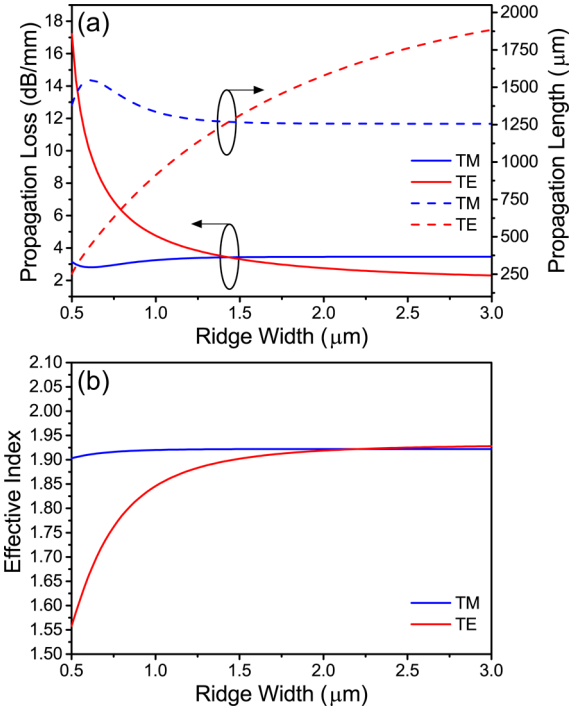

Figure 2. (a) Propagation loss and corresponding propagation length for the TE and TM modes as a function of the ridge width, w_{ridge}. (b) Effective index of the TE and TM modes as a function of the ridge width, w_{ridge}. Note the phase-matching condition is satisfied at w_{ridge} = 2.2 μm. In both (a) and (b), w = 450 nm, t_{ridge} = 320 nm, $t_{Bi:YIG}$ = 260 nm, t_{SiO_2} = 20 nm, t_{Ag} = 25 nm, and t_{TiO_2} = 725 nm.

tuning the modes to achieve phase matching without requiring complex periodic structural or magnetic variations. Typically, altering a waveguide dimension impacts the effective index for both TE and TM modes ($n_{eff,TE}$ and $n_{eff,TM}$), and thus they cannot be tailored individually. However, here the TM plasmonic mode is confined near the Ag film, while the TE photonic mode is contained within the ridge. Since the TM mode fields do not significantly extend into the ridge, adjusting the ridge width, w_{ridge}, allows the effective index of the TE mode to be tuned almost independently from that of the TM mode, as shown in Figure 2b. In the present configuration, w_{ridge} is chosen to be 2.2 μm, corresponding to the crossing point of the curves in Figure 2b.

The proposed magnetoplasmonic Faraday rotators can be fabricated in any well-equipped facility. The high-quality magnetic garnet films can be deposited onto SiO_2 via pulsed laser deposition (PLD),[36] while the thin SiO_2 films and the Ag film can be deposited with plasma-enhanced chemical vapor deposition (PECVD) and sputtering, respectively. Amorphous TiO_2 can then be reactively sputtered as the top layer. Electron beam lithography and focused ion beam (FIB) milling can accurately shape the structure. Notably, it is common for devices relying on phase-matched modes to possess strict fabrication tolerances. However, this is alleviated in the hybrid ridge−plasmonic design, due to the independent tuning of the TE mode effective index. One can fabricate the structure with an exaggerated w_{ridge}, characterize the resulting $n_{eff,TM}$

DOI: 10.1021/acsphotonics.6b00523
ACS Photonics 2016, 3, 2344−2352

accounting for fabrication defects in the multilayer stack, and then selectively mill the ridge via FIB to achieve precise phase matching.

After fabrication, a suitable experimental coupling scheme must be chosen to allow the light to be coupled into/out of the device at the different locations on the waveguide cross section to maximize coupling efficiency, due to the offset modal centers of the TE and TM modes. Some examples include piezo-mounted fiber coupling or the design of appropriate coupling waveguides. One must also account for the difference in external coupling efficiencies arising from the variation in modal field distribution between the TE and TM modes, which clearly is highly dependent on the coupling scheme employed. When the light is coupled into the proposed ridge plasmonic waveguide, the coupling efficiency can be optimized by matching the spatial and phase profiles of the modes of the input waveguide to the MO waveguide. Such a phase-matching technique has shown to be efficient to transfer energy from a silicon nanowire to the plasmonic waveguide, even though their mode sizes are significantly different.[37,38] Because the effective index difference between TE-photonic and TM-plasmonic modes has been minimized due to the phase match condition required for a magnetoplasmonic Faraday rotator, one can thus judiciously design the input waveguide such that its phase velocity is matched to the ridge−plasmonic waveguide.

Theoretical treatment describing Faraday rotation within waveguides[39] predicts that mode separation degrades the power conversion efficiency and increases the conversion length. However, this drop in conversion efficiency can be remedied with sufficient phase matching. For the TE and TM modes of this structure, the effective index difference is $\Delta n_{\text{eff}} = |n_{\text{eff,TM}} - n_{\text{eff,TE}}| = 4 \times 10^{-5}$. Thus, the conversion efficiency and conversion length are predicted to be 99.8% and $L_{\text{conv}} = 819$ μm, respectively. Correspondingly, in this configuration, the propagation lengths of the two modes are $L_{\text{prop,TM}} = 1257$ μm and $L_{\text{prop,TE}} = 1660$ μm, as shown in Figure 2a, leading to relatively low insertion loss (2.5 dB) compared to other plasmonic structures.[12,18,20] Note that this value can be further optimized by either reducing the thickness of the metal layer or restructuring the hybrid plasmonic section such that the phase-matching condition corresponds to a wider ridge width. Clearly, this unique structure allows the simultaneous implementation of long-range phase-matched eigenmodes, which are ideal for demonstrating the Faraday effect.

To investigate the Faraday rotation of the device, we employ fully vectorial finite-difference-time-domain (FDTD) simulations. Here, the desired input mode is directly injected into the waveguide, while the magnetization of the Bi:YIG is accounted for with a full gyrotropic permittivity tensor:[40]

$$\varepsilon_r(\mathbf{M}) = \begin{bmatrix} n^2_{\text{Bi:YIG}} & -ig_z & ig_y \\ ig_z & n^2_{\text{Bi:YIG}} & -ig_x \\ -ig_y & ig_x & n^2_{\text{Bi:YIG}} \end{bmatrix} \quad (1)$$

Here, $\mathbf{g}(\mathbf{M}) = \langle g_x, g_y, g_z \rangle$ denotes the gyration vector of the Bi:YIG, whose elements are given by the following:[40]

$$g_j = -\frac{\lambda n_{\text{Bi:YIG}}}{\pi}\frac{M_j}{M_S}\theta_F(\lambda) \quad (2)$$

where $j = x, y, z$ and $\mathbf{M} = \langle M_x, M_y, M_z \rangle$ is the Bi:YIG's magnetization vector. In the present geometry, Faraday rotation is observed when the $\mathbf{M}$ is parallel to the propagation direction (i.e., the y-axis), and thus we consider $\mathbf{M} = \langle 0, +M_S, 0 \rangle$, induced by a parallel static magnetic field vector ($\mathbf{H}_{\text{static}} = \langle 0, +H_y, 0 \rangle$) as shown in Figure 1a. Thus, $g_y = -5.0 \times 10^{-3}$ for the Bi:YIG at $\lambda = 1.55$ μm. The local normalized power in each of the modes as a function of device length is plotted in Figure 3a for a TM input and in Figure 3b for a TE input at $\lambda = 1.55$ μm. Here we adopt an experimentally measurable definition of the power, such that P_{TM} and P_{TE} are the integrated TM and TE contributions to the y-component of the Poynting vector, $S_y = 0.5(E_z H_x^* - E_x H_z^*)$, over the cross sectional area, A:

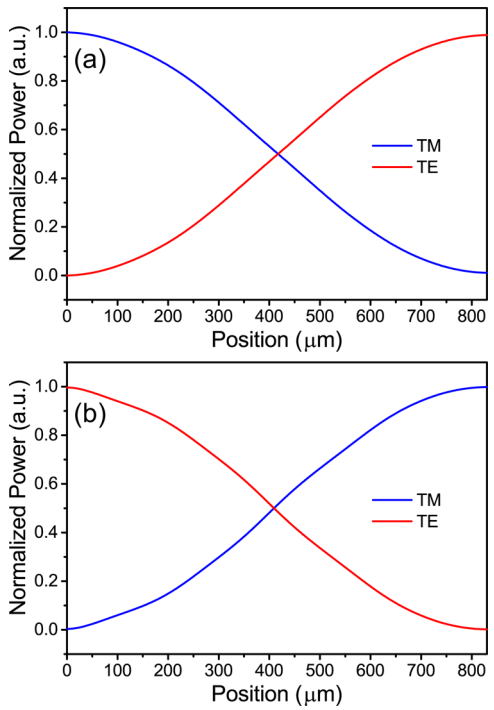

Figure 3. Normalized power in each of the TE and TM components along the length of the device for (a) a TM input or (b) a TE input into the device depicted in Figure 1.

$$P_{\text{TM}} = \frac{1}{2}\text{Re}\left(\iint E_z H_x^* dA\right)$$
$$P_{\text{TE}} = -\frac{1}{2}\text{Re}\left(\iint E_x H_z^* dA\right) \quad (3)$$

Thus, the local normalized power in each cross section along the device length is given by

$$P_{\text{TM,norm}} = \frac{P_{\text{TM}}}{P_{\text{TM}} + P_{\text{TE}}}$$
$$P_{\text{TE,norm}} = \frac{P_{\text{TE}}}{P_{\text{TM}} + P_{\text{TE}}} \quad (4)$$

As evident from Figure 3, a power conversion efficiency of 99.4% is attained within a conversion length of $L_{\text{conv}} = 830$ μm when either a TE or TM mode is launched into the device. These values agree with the theoretical predictions within 0.4% and 1.3%, respectively. Notably, the unique hybridization of the field-balanced plasmonic structure and conventional ridge waveguides facilitates sufficiently low losses, such that L_{conv} is significantly less than the propagation lengths of the TE or TM

DOI: 10.1021/acsphotonics.6b00523
ACS Photonics 2016, 3, 2344−2352

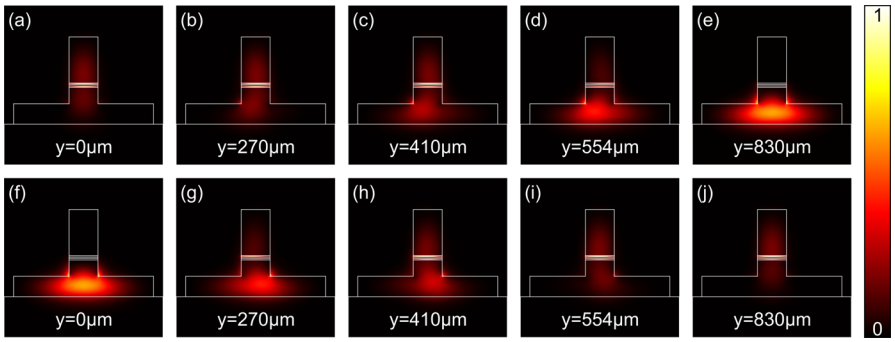

Figure 4. $|E|^2$ profiles within the device for (a–e) a TM input and (f–j) a TE input. (a) and (f) depict the input modes at $y = 0$ μm, (b) and (g) depict the fields at $y = 270$ μm, where 25% conversion has occurred, (c) and (h) depict the fields at $y = 410$ μm, where 50% conversion has occurred, (d) and (i) depict the fields at $y = 554$ μm, where 75% conversion has taken place, and (e) and (j) depict the output field profiles, at $y = L_{conv} = 830$ μm. Note that the color scale of each frame is normalized between 0 and 1 to clearly depict the mode evolution.

modes, and high efficiency conversion can be attained within the plasmonic device. Cross-sectional profiles of $|E|^2$ within the waveguide at five locations along the device are depicted in Figure 4 (i.e., $y = 0$ μm, $y = 270$ μm, $y = 410$ μm, $y = 554$ μm, and $y = 830$ μm). For a plasmonic TM mode input (Figure 4a–e), one can clearly observe the $|E|^2$ profile evolving from the dominantly E_z distribution around the metal film (see Figure 1c) into the E_x distribution contained within the ridge (see Figure 1d) at the device output ($y = L_{conv} = 830$ μm). Conversely, for a photonic TE mode input (Figure 4f–j), the dominant E_x fields (see Figure 1d) evolve into a symmetric E_z field distribution (see Figure 1c) around the Ag film at the device output ($y = L_{conv} = 830$ μm).

Clearly, this magnetoplasmonic device is ideal for polarization diversity circuits, as it is versatile enough to handle either input polarization state and can convert between tightly confined modes ideal for integrated optics applications. Additionally, with future developments in the fabrication of Bi:YIG films, one will be able to employ films with larger values of θ_F and hence attain complete mode conversion within a much shorter device length.

In addition to magnetoplasmonic effects, the hybrid ridge–plasmonic waveguide represents a robust design methodology to achieve any integrated plasmonic functionalities that involve phase-matching engineering. One prominent example that can directly benefit from this architecture is the design of integrated nonlinear plasmonic waveguides.[41] Typically, the plasmonic mode at the fundamental frequency is selected to generate a photonic mode at the signal frequency through a nonlinear process.[42,43] Similar to the performance metrics obtained for Faraday rotation, an optimized nonlinear plasmonic waveguide requires a delicate balance between the modal losses and the appreciable modal overlap to ensure an efficient mode conversion. Through the utilization of hybrid ridge–plasmonic structure, one can replace Bi:YIG by other nonlinear materials (e.g., $LiNbO_3$) and attain birefringence phase matching by including the geometrical and material dispersions.

■ ACTIVE POLARIZATION CONTROL

A unique feature arising from the implementation of a magnetoplasmonic Faraday rotator is the ability to actively control the fraction of power in each of the TE and TM components at the device output. This is possible as the Faraday rotation is induced by the magnetization of the Bi:YIG, and **M** itself can be dynamically modified by transient magnetic field pulses. This concept was demonstrated previously in a class of devices employing dynamic actuation of the nonreciprocal phase shift.[44,45] In an altered configuration, when current signals are made to propagate through a metal feature in close proximity to the Bi:YIG, the generated magnetic fields can be made to actively modulate the polarization state of the lightwave.

In the present geometry, active modulation is achieved through a Ag transmission line (TL), buried $d = 1.5$ μm below the surface of the SiO_2. This structure has dimensions of $w_{TL} = 8$ μm and $t_{TL} = 1.5$ μm, runs along the length of the device, and is set in contact with a Si substrate for heat sinking. In this orientation, super-Gaussian current pulses with a peak of 1A will generate transient fields, $\mathbf{h}(t) = \langle h_x(t), 0, 0\rangle$, over the Bi:YIG, where the peak magnetic field is about $\mu_0 h_{x,pk} = 51$ mT. This in turn modulates **M** in accordance with the Landau–Lifshitz–Gilbert (LLG) model of magnetization dynamics:[46]

$$\frac{d\mathbf{M}}{dt} = -\frac{\mu_0\gamma_0}{1+\alpha^2}[\mathbf{M}\times(\mathbf{H}_{static}+\mathbf{h}(t))] - \frac{\mu_0\gamma_0\alpha}{M_S(1+\alpha^2)}\mathbf{M}\times[\mathbf{M}\times(\mathbf{H}_{static}+\mathbf{h}(t))] \quad (5)$$

where μ_0 is the permeability of free space and γ_0 is the gyromagnetic ratio. In the following sections, it is shown that the magnetoplasmonic Faraday rotator can be operated in two different dynamic modes, depending on the orientation of the static biasing field, $\mathbf{H}_{static}$. If $\mathbf{H}_{static}$ is aligned with the y-axis, $\mathbf{H}_{static} = \langle 0, +H_y, 0\rangle$, the device can be operated in a pulsed-input pulsed-output (PIPO) mode, whereby the appropriate choice of magnetic field parameters can map individual magnetic field pulses onto the magnetization and, thus, onto the polarization state. Conversely, if $\mathbf{H}_{static}$ is aligned with the z-axis, $\mathbf{H}_{static} = \langle 0, 0, +H_z\rangle$, the device can be operated in a pulsed-input continuous-output (PICO) mode, where a single magnetic field pulse excites an oscillation within the Bi:YIG and hence maps the decaying oscillation onto the output polarization state.

Pulsed-Input Pulsed-Output Operation. The mechanism of control employed here is based on magnetic precession within the Bi:YIG. When the magnetic field in the Bi:YIG is not aligned with **M**, eq 5 dictates that **M** will begin to precess around the magnetic field vector. The amplitude of this precession gradually diminishes until the two vectors are in alignment, while the frequency is given by the Larmor frequency:[46]

DOI: 10.1021/acsphotonics.6b00523
ACS Photonics 2016, 3, 2344–2352

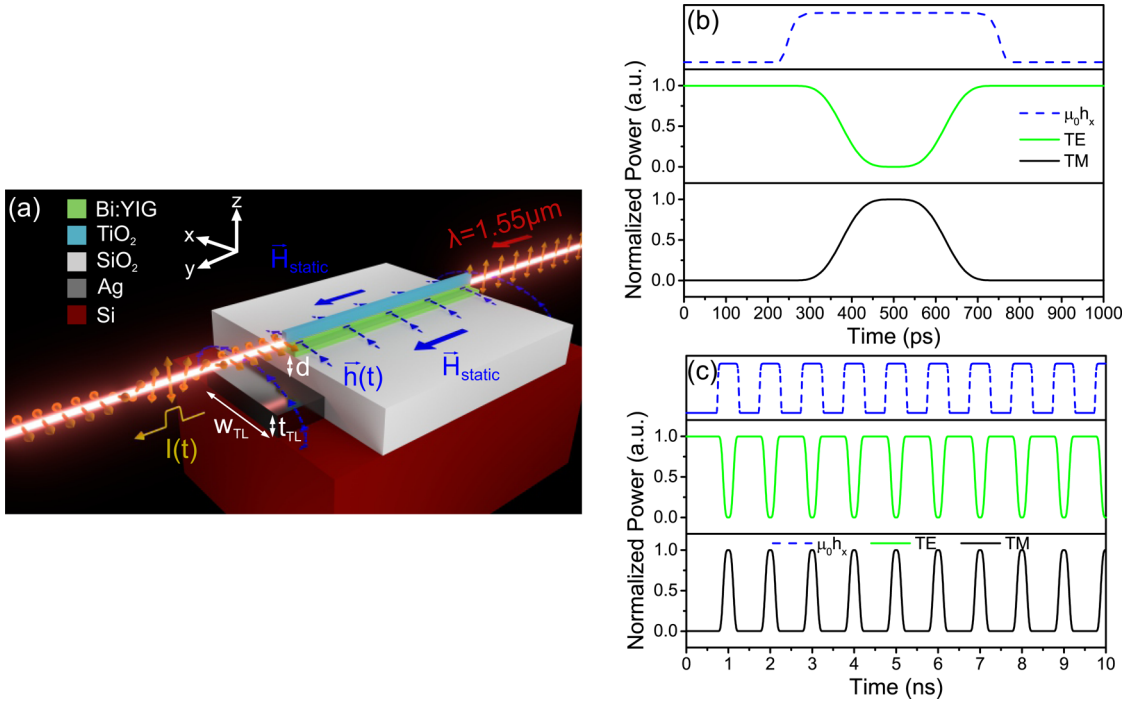

Figure 5. (a) Schematic illustration of the geometry required for the pulsed-input pulsed-output (PIPO) dynamic operation mode. (b, c) Operation of the device in PIPO mode, with a TM input. (b) Polarization switching due to a single input pulse with τ_p = 500 ps, $\mu_0 h_{x,pk}$ = 51 mT, and $\mu_0 H_y$ = 51 mT. The device acts as an "on"-to-"off" switch. (c) Polarization response to a train of these input pulses at a repetition rate of f_{rep} = 1 GHz. Note that the $\mu_0 h_x$ curves are not to scale and are only intended to indicate the timing.

$$\nu = \frac{\gamma_0}{2\pi}\mu_0|\mathbf{H}_{static} + \mathbf{h}(t)| \quad (6)$$

A schematic illustration of the geometry required for PIPO operation is shown in Figure 5a. A static magnetic field, $\mathbf{H}_{static} = \langle 0, +H_y, 0\rangle$, is externally applied to the device to initially set $\mathbf{M}$ to a known state, $\mathbf{M}_0 = \langle 0, +M_S, 0\rangle$. When the transient magnetic field, $\mathbf{h}(t) = \langle h_x(t), 0, 0\rangle$, is applied, the two vectors are not aligned, and hence $\mathbf{M}$ begins to precess around $\mathbf{H}_{static} + \mathbf{h}(t)$. Following this excitation, when $\mathbf{h}(t)$ is turned off, $\mathbf{M}$ will precess around $\mathbf{H}_{static}$ alone. In the present configuration, this implies that $\mathbf{M}$ is deflected away from the y-axis by $\mathbf{h}(t)$ and then begins to precess around it as it slowly relaxes.[44,45]

Notably, it is the M_y component that induces the Faraday effect and hence is mapped onto the polarization of the lightwave at the device output. To induce one-to-one pulse mapping between the driving electrical pulse and the optical polarization state, this oscillatory precession amplitude must be minimized, or correspondingly, we require H_y, $h_{x,pk}$, and the pulse width τ_p to be judicially chosen such as to return $\mathbf{M}$ to its initial state at the conclusion of $\mathbf{h}(t)$.[44] With these conditions satisfied, the waveguide will switch the polarization rotation from "on" to "off" and back again.

As an example, this functionality can be achieved by employing τ_p = 500 ps pulses with a peak magnetic field of $\mu_0 h_{x,pk}$ = 51 mT and a static biasing field of $\mu_0 H_y$ = 51 mT. The local normalized power at the device output is shown in Figure 5b for a TM input to the device. Note that since the device is an "on"-to-"off" switch, the TM input switches the output polarization state from TE to TM and back. These parameters achieve a polarization modulation depth of >99% in the output state.

Additionally, this device can respond to a train of the above specified electrical input pulses to encode binary data onto the polarization state of the guided optical mode. Figure 5c depicts the output of the device under excitation from a train of electrical pulses at a repetition rate of f_{rep} = 1 GHz. Note that analogous operation is achieved for a TE input to the device as well. Such polarization modulation can easily be converted to optical intensity modulation through the use of a polarizer. Clearly, the polarization rotation can be switched in a regular manner with the above parameters and, as such, provides an efficient means of mapping an electrical excitation onto the polarization state.

Pulsed-Input Continuous-Output Operation. While the PIPO mode required suppression of the precessional oscillations within the Bi:YIG, changing the orientation of $\mathbf{H}_{static}$ allows for PICO operation. Unlike the dynamic nonreciprocal phase modulation employed previously,[45] the present device allows for the excitation of high-speed oscillations in the output polarization state. In this configuration, shown in Figure 6a, the static biasing magnetic field is oriented along the z-axis, $\mathbf{H}_{static} = \langle 0, 0, +H_z\rangle$, to initially set $\mathbf{M}$ in the same direction. Applying the transient pulse $\mathbf{h}(t) = \langle h_x(t), 0, 0\rangle$ deflects $\mathbf{M}$ away from the z-axis, around which it begins to precess at the Larmor frequency, ν. Thus, the Faraday rotation within the device exhibits similar oscillatory behavior to that of M_y. As $\mathbf{M}$ revolves around the z-axis, the sinusoidal variations in M_y (and by extension θ_F) occur at ν. However, since the fraction of power contained in the TE and TM components at the device output do not depend on the sign of θ_F, the power carried in each of the TE and TM components will oscillate at a frequency of 2ν. Thus, a single magnetic field pulse can excite long-lasting high-frequency modulation of the output polarization state.

In order to maximize the polarization modulation depth, one requires the magnetic field pulse to excite the largest amplitude precession about the z-axis possible. Clearly, since $|\mathbf{M}| = M_S$ is

DOI: 10.1021/acsphotonics.6b00523
ACS Photonics 2016, 3, 2344−2352

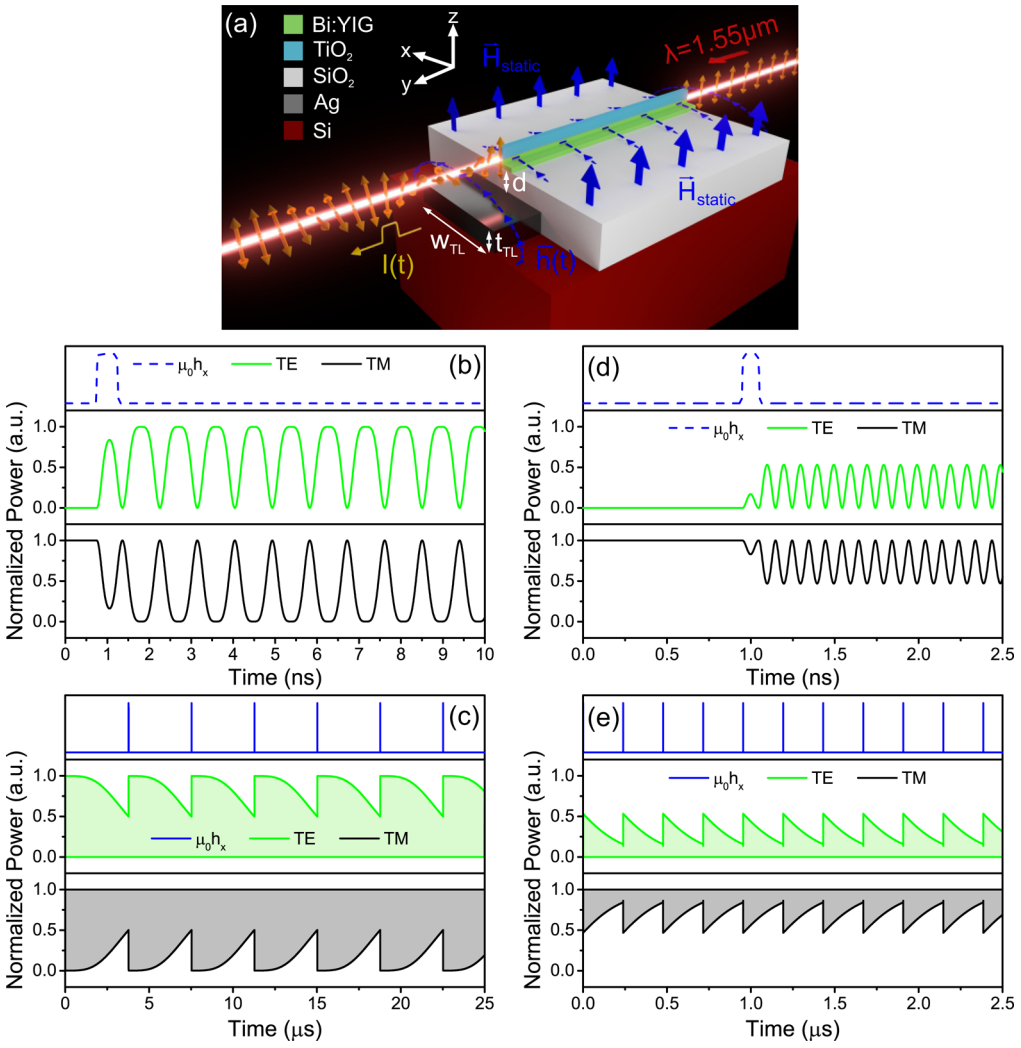

Figure 6. (a) Schematic illustration of the geometry required for the pulsed-input continuous-output (PICO) dynamic operation mode. (b–e) Operation of the device in PICO mode with a TM input. (b) 2ν = 1.12 GHz oscillating polarization response induced by a single magnetic field pulse with τ_p = 500 ps, $\mu_0 h_{x,pk}$ = 22 mT, and $\mu_0 H_z$ = 20 mT. Note that the amplitude of this oscillation decays on a microsecond time scale. (c) Decaying envelope of the polarization response due to the aforementioned magnetic field pulses repeated at f_{rep} = 267 kHz. (d) 2ν = 10.08 GHz oscillating polarization response induced by a single magnetic field pulse with τ_p = 100 ps, $\mu_0 h_{x,pk}$ = 51 mT, and $\mu_0 H_z$ = 180 mT. Note that the amplitude of this oscillation decays on a time scale of a few hundred nanoseconds. (e) Decaying envelope of the polarization response due to the aforementioned magnetic field pulses repeated at f_{rep} = 4.2 MHz. Note that within the shaded region the polarization oscillations occur on a time scale of nanoseconds in (c) or a few hundred picoseconds in (e) and thus cannot be observed here. In (b)–(e), the $\mu_0 h_x$ curves are not to scale and are only intended to indicate the timing.

constant, this can be achieved if the transient pulse excites **M** to a state such that M_z/M_S = 0. By appropriately selecting the operating biasing field (H_z), peak transient field ($h_{x,pk}$), and pulse width (τ_p), one can realize this condition. One such example is depicted in Figure 6b, which plots the temporal variations in the local normalized power at the device output for τ_p = 500 ps, $\mu_0 h_{x,pk}$ = 22 mT, and $\mu_0 H_z$ = 20 mT. For this biasing field, ν = 560 MHz, but the power contained within the TE and TM components oscillates at 2ν = 1.12 GHz. Such an oscillatory behavior decays on a time scale of microseconds. The repetition rate, f_{rep}, of the input electrical pulses can be very low to drive this continuous oscillation. Adopting the re-excitation threshold defined in ref 45, whereby the device is stimulated by a new pulse when the precession amplitude decays to 50% of its initial value, this device can be driven at the low repetition rate of f_{rep} = 267 kHz. This operation is depicted in Figure 6c. Thus, the frequency of the output polarization state oscillations is about 4.2×10^3 times greater than the input repetition rate.

Higher modulation frequencies can be achieved, as Bi:YIG has demonstrated responses of 82 GHz.[35] However, in order to achieve higher output frequencies in the PICO mode, one must utilize higher static fields (to increase ν) and, correspondingly, shorter pulse widths.[45] As a consequence, one must sacrifice modulation depth to avoid unwieldy increases in the current requirements. For example, the output of the device is plotted as a function of time for a device driven with τ_p = 100 ps pulses with an amplitude of $\mu_0 h_{x,pk}$ = 51 mT, under a static bias of $\mu_0 H_z$ = 180 mT, in Figure 6d. In this scenario, ν = 5.04 GHz, and correspondingly, the polarization state oscillates at 2ν = 10.08 GHz. However, the modulation depth is reduced to 53%. These rapid oscillations decay much quicker, so the repetition rate required by the aforementioned threshold is f_{rep} = 4.2 MHz, as shown in Figure 6e. Correspondingly, the frequency of

DOI: 10.1021/acsphotonics.6b00523
ACS Photonics 2016, 3, 2344–2352

the oscillating polarization at the output is 2.4×10^3 times greater than the input modulation frequency.

Clearly, by orienting the static magnetic field appropriately, one can advantageously employ the inherent ferromagnetic resonance of the Bi:YIG to generate continuous high-frequency polarization modulation for low repetition rate input excitations.

CONCLUSIONS

In conclusion, we have presented a unique hybrid ridge−plasmonic Faraday rotator. Such a geometry facilitates the implementation of long-range phase-matched photonic TE and plasmonic TM modes. By employing Bi:YIG within this structure, the magnetized device converts between the two modes via the Faraday effect. With the inclusion of a nearby metallic transmission line to generate transient magnetic fields, the magnetization of the Bi:YIG, and thus the output polarization state, can be effectively manipulated. The device is operable in two dynamic modes, mapping electrical pulses onto the output polarization state or generating continuous polarization oscillations. As such, this device presents a unique and versatile platform for polarization control in integrated plasmonics. The described architecture facilitates high-speed integrated plasmonic−photonic polarization control, is tunable to achieve a wide range of modulation frequencies, and is robust enough to function with either TE or TM input. Therefore, this magnetoplasmonic Faraday rotator can facilitate polarization division multiplexing and polarization encoding within nanoplasmonic circuitry and will be a fundamental building block within future nanoplasmonic optical networks.

AUTHOR INFORMATION

Corresponding Author

*E-mail: firby@ualberta.ca.

ORCID

Curtis J. Firby: 0000-0002-3128-3758

Notes

The authors declare no competing financial interest.

ACKNOWLEDGMENTS

This work was funded by the Natural Sciences and Engineering Research Council of Canada.

REFERENCES

(1) Hayee, M. I.; Cardakli, M. C.; Sahin, A. B.; Willner, A. E. Doubling of bandwidth utilization using two orthogonal polarizations and power unbalancing in a polarization-division-multiplexing scheme. *IEEE Photonics Technol. Lett.* **2001**, *13*, 881−883.

(2) Wang, S. Y.; Lin, S. H.; Houng, Y. M. GaAs traveling-wave polarization electro-optic waveguide modulator with bandwidth in excess of 20 GHz at 1.3μm. *Appl. Phys. Lett.* **1987**, *51*, 83−85.

(3) Irvine, S. E.; Elezzabi, A. Y. Wideband magneto-optic modulation in a bismuth-substituted yttrium iron garnet waveguide. *Opt. Commun.* **2003**, *220*, 325−329.

(4) Dai, D.; Liu, L.; Gao, S.; Xu, D.-X.; He, S. Polarization management for silicon photonic integrated circuits. *Laser Photonics Rev.* **2013**, *7*, 303−328.

(5) Dai, D.; Bauters, J.; Bowers, J. E. Passive technologies for future large-scale photonic integrated circuits on silicon: polarization handling, light non-reciprocity and loss reduction. *Light: Sci. Appl.* **2012**, *1*, e1.

(6) Ding, F.; Wang, Z.; He, S.; Shalaev, V. M.; Kildishev, A. V. Broadband high-efficiency half-wave plate: a supercell-based plasmonic metasurface approach. *ACS Nano* **2015**, *9*, 4111−4119.

(7) Jiang, Z. H.; Lin, L.; Ma, D.; Yun, S.; Werner, D. H.; Liu, Z.; Mayer, T. S. Broadband and wide field-of-view plasmonic metasurface-enabled waveplates. *Sci. Rep.* **2014**, *4*, 7511.

(8) Roberts, A.; Lin, L. Plasmonic quarter-wave plate. *Opt. Lett.* **2012**, *37*, 1820−1822.

(9) Li, J.; Chen, S.; Yang, H.; Li, J.; Yu, P.; Cheng, H.; Gu, C.; Chen, H.-T.; Tian, J. Simultaneous control of light polarization and phase distributions using plasmonic metasurfaces. *Adv. Funct. Mater.* **2015**, *25*, 704−710.

(10) Chang, P.; Lin, C.; Helmy, A. S. Polarization engineering in nanoscale waveguides using lossless media. *J. Lightwave Technol.* **2016**, *34*, 952−960.

(11) Brooks, C.; Jessop, P. E.; Deng, H.; Yevick, D. O.; Tarr, G. Passive silicon-on-insulator polarization-rotating waveguides. *Opt. Eng.* **2006**, *45*, 044603.

(12) Zhang, J.; Zhu, S.; Zhang, H.; Chen, S.; Lo, G.-Q.; Kwong, D.-L. An ultracompact surface plasmon polariton-effect-based polarization rotator. *IEEE Photonics Technol. Lett.* **2011**, *23*, 1606−1608.

(13) Chang, Y.-J.; Yu, T.-H. Photonic-quasi-TE-to-hybrid-plasmonic-TM polarization mode converter. *J. Lightwave Technol.* **2015**, *33*, 4261−4267.

(14) Kim, S.; Qi, M. Mode-evolution-based polarization rotation and coupling between silicon and hybrid plasmonic waveguides. *Sci. Rep.* **2015**, *5*, 18378.

(15) Caspers, J. N.; Alam, M. Z.; Mojahedi, M. Compact hybrid plasmonic polarization rotator. *Opt. Lett.* **2012**, *37*, 4615−4617.

(16) Caspers, J. N.; Aitchison, J. S.; Mojahedi, M. Experimental demonstration of an integrated hybrid plasmonic polarization rotator. *Opt. Lett.* **2013**, *38*, 4054−4057.

(17) Jin, L.; Chen, Q.; Wen, L. Mode-coupling polarization rotator based on a plasmonic waveguide. *Opt. Lett.* **2014**, *39*, 2798−2801.

(18) Hassan, K.; Leroy, F.; Colas-des-Francs, G.; Weeber, J.-C. Dihedron dielectric loaded surface plasmon athermal polarization converter. *Opt. Lett.* **2014**, *39*, 697−700.

(19) Kim, S.; Qi, M. Polarization rotation and coupling between silicon waveguide and hybrid plasmonic waveguide. *Opt. Express* **2015**, *23*, 9968−9978.

(20) Gao, L.; Huo, Y.; Zang, K.; Paik, S.; Chen, Y.; Harris, J. S.; Zhou, Z. On-chip plasmonic waveguide optical waveplate. *Sci. Rep.* **2015**, *5*, 15794.

(21) Okamura, Y.; Chatani, M.; Kikuchi, T.; Yamamoto, S. Polarization mode conversion in YIG rib waveguide. *Opt. Quantum Electron.* **1985**, *17*, 427−430.

(22) Armelles, G.; Cebollada, A.; García-Martín, A.; González, M. U. Magnetoplasmonics: combining magnetic and plasmonic functionalities. *Adv. Opt. Mater.* **2013**, *1*, 10−35.

(23) Hu, B.; Zhang, Y.; Wang, Q. J. Surface magneto plasmons and their applications in the infrared frequencies. *Nanophotonics* **2015**, *4*, 383−396.

(24) Chin, J. Y.; Steinle, T.; Wehlus, T.; Dregely, D.; Weiss, T.; Belotelov, V. I.; Stritzker, B.; Giessen, H. Nonreciprocal plasmonics enables giant enhancement of thin-film Faraday rotation. *Nat. Commun.* **2013**, *4*, 1599.

(25) Floess, D.; Chin, J. Y.; Kawatani, A.; Dregely, D.; Habermeier, H.-U.; Weiss, T.; Giessen, H. Tunable and switchable polarization rotation with non-reciprocal plasmonic thin films at designated wavelengths. *Light: Sci. Appl.* **2015**, *4*, e284.

(26) Uchida, H.; Masuda, Y.; Fujikawa, R.; Baryshev, A. V.; Inoue, M. Large enhancement of Faraday rotation by localized surface plasmon resonance in Au nanoparticles embedded in Bi:YIG film. *J. Magn. Magn. Mater.* **2009**, *321*, 843−845.

(27) Khanikaev, A. B.; Baryshev, A. V.; Fedyanin, A. A.; Granovsky, A. B.; Inoue, M. Anomalous Faraday effect of a system with extraordinary optical transmittance. *Opt. Express* **2007**, *15*, 6612−6622.

(28) Caballero, B.; García-Martín, A.; Cuevas, J. C. Faraday effect in hybrid magneto-plasmonic photonic crystals. *Opt. Express* **2015**, *23*, 22238−22249.

DOI: 10.1021/acsphotonics.6b00523
ACS Photonics 2016, 3, 2344−2352

(29) Ma, W.; Helmy, A. S. Asymmetric long-range hybrid-plasmonic modes in asymmetric nanometer-scale structures. *J. Opt. Soc. Am. B* **2014**, *31*, 1723−1729.
(30) Johnson, P. B.; Christy, R. W. Optical constants of noble metals. *Phys. Rev. B* **1972**, *6*, 4370−4379.
(31) Palik, E. D. *Handbook of Optical Constants of Solids*; Academic Press: San Diego, 1998.
(32) Bradley, J. D. B.; Evans, C. C.; Choy, J. T.; Reshef, O.; Deotare, P. B.; Parsy, F.; Phillips, K. C.; Lončar, M.; Mazur, E. Submicrometer-wide amorphous and polycrystalline anatase TiO_2 waveguides for microphotonic devices. *Opt. Express* **2012**, *20*, 23821−23831.
(33) Irvine, S. E.; Elezzabi, A. Y. Modeling of high-speed magnetooptic beam deflection. *IEEE J. Quantum Electron.* **2002**, *38*, 1428−1435.
(34) Kurebayashi, H.; Dzyapko, O.; Demidov, V. E.; Fang, D.; Ferguson, A. J.; Demokritov, S. O. Controlled enhancement of spin-current emission by three-magnon splitting. *Nat. Mater.* **2011**, *10*, 660−664.
(35) Elezzabi, A. Y.; Freeman, M. R. Ultrafast magnetooptic sampling of picosecond current pulses. *Appl. Phys. Lett.* **1996**, *68*, 3546−3548.
(36) Bi, L.; Hu, J.; Jiang, P.; Kim, D. H.; Dionne, G. F.; Kimerling, L. C.; Ross, C. A. On-chip optical isolation in monolithically integrated non-reciprocal optical resonators. *Nat. Photonics* **2011**, *5*, 758−762.
(37) Lin, C.; Wong, H. M. K.; Lau, B.; Swillam, M. A.; Helmy, A. S. Efficient broadband energy transfer via momentum matching at hybrid junctions of guided-waves. *Appl. Phys. Lett.* **2012**, *101*, 123115.
(38) Lau, B.; Swillam, M. A.; Helmy, A. S. Hybrid orthogonal junctions: wideband plasmonic slow-silicon waveguide couplers. *Opt. Express* **2010**, *18*, 27048−27059.
(39) Yamamoto, S.; Koyamada, Y.; Makimoto, T. Normal-mode analysis of anisotropic and gyrotropic thin-film waveguides for integrated optics. *J. Appl. Phys.* **1972**, *43*, 5090−5097.
(40) Zvezdin, A. K.; Kotov, V. A. *Modern Magnetooptics and Magnetooptical Materials*; IOP Publishing: Bristol, 1997.
(41) Kauranen, M.; Zayats, A. V. Nonlinear plasmonics. *Nat. Photonics* **2012**, *6*, 737−748.
(42) Lu, F. F.; Li, T.; Hu, X. P.; Cheng, Q. Q.; Zhu, S. N.; Zhu, Y. Y. Efficient second-harmonic generation in nonlinear plasmonic waveguide. *Opt. Lett.* **2011**, *36*, 3371−3373.
(43) Pigozzo, F. M.; Modotto, D.; Wabnitz, S. Second harmonic generation by modal phase matching involving optical and plasmonic modes. *Opt. Lett.* **2012**, *37*, 2244−2246.
(44) Firby, C. J.; Elezzabi, A. Y. High-speed nonreciprocal magnetoplasmonic waveguide phase shifter. *Optica* **2015**, *2*, 598−606.
(45) Firby, C. J.; Elezzabi, A. Y. A magnetoplasmonic electrical-to-optical clock multiplier. *Appl. Phys. Lett.* **2016**, *108*, 051111.
(46) Soohoo, R. F. *Microwave Magnetics*; Harper & Row: New York, 1985.

DOI: 10.1021/acsphotonics.6b00523
ACS Photonics 2016, 3, 2344−2352